Selective coupling and decoupling coordinate distributed brain networks for precise action

Stefan M. Lemke[1✉], Simone Appaqaq[1], Jian-Zhong Guo[1*], Adam W. Hantman[1*✉]

[1] Neuroscience Center and Department of Cell Biology & Physiology, University of North Carolina at Chapel Hill, USA.

[*] J-Z.G. and A.W.H. are co-senior authors.

✉ Correspondence: stefan.lemke@unc.edu (S.M.L.), adam_hantman@unc.edu (A.W.H.)

Abstract

The mammalian brain is fundamentally interconnected. Across species, a single neuron typically forms thousands of synapses spanning local and long-range connections. This architecture suggests that brain function is distributed, but it remains poorly understood how relevant networks are selectively engaged to produce appropriate behaviors. To address this, we recorded >40,000 neurons, simultaneously monitoring five cerebellar and cerebral brain areas as mice performed complex motor actions, capturing interactions of >5,000,000 cross-area neuron pairs. This revealed that complex pre-movement cross-area interactions coordinate distributed networks to produce precise and consistent actions. Prior to action production, action-informative neural populations across the brain become coupled, while non-informative populations decouple. This coupling and decoupling was mirrored by two distinct local field potential oscillations linking neuron-level to population-level dynamics. External modulation of these dynamics revealed their necessity for skilled action. Our work highlights that a complex pre-movement orchestration of coupling and decoupling ensures the selective engagement of relevant distributed networks to produce precise action.

Introduction

In the mammalian brain, individual neurons contact hundreds to thousands of local and distant neuron partners, forming highly distributed networks[1–6]. Consistent with this architecture, neural activity across cerebral and cerebellar areas is broadly modulated during salient behavioral events such as purposeful movements[7–10]. To produce a specific behavior, relevant neurons distributed across the brain must be coordinated to generate appropriate patterns of activity. The principles by which these neurons interact to enable precise and consistent behavior are poorly defined.

The control of skilled motor actions exemplifies this challenge. Control of a skilled reaching and grasping action relies on contributions from neurons across the brain, evidenced by impaired performance following disruptions to either cerebral cortex[11–15], thalamus[16], basal ganglia[11,13], or cerebellum[17–19]. Determining how these neurons are coordinated requires simultaneous multi-site neurophysiology to identify action-informative neurons in each area and measure their interactions during action production. Measuring interactions between action-informative neurons is essential, as overall neural population dynamics can fail to capture task-relevant dynamics[9,20–23].

Here, we recorded >40,000 neurons, simultaneously monitoring frontal and motor cortical areas, dorsal striatum, motor thalamus, and cerebellum as mice generated reach-to-grasp actions, isolating distributed networks of action-informative and non-informative neurons. We examined the interaction of >5,000,000 cross-area neuron pairs to find that in the ~10s preceding action production, a balance of coupling among action-informative neurons and decoupling among non-informative neurons ensured that upcoming actions were precise and consistent. We identified two oscillatory rhythms that linked these neuron-level dynamics to population-level dynamics and, by optogenetically manipulating them, established their necessity for skilled action. These results reveal that selective coupling and decoupling coordinate distributed brain networks to produce skilled actions.

Results

Action information and modulation are widely distributed across the brain.

To investigate how distributed brain areas contribute to skilled motor control, we trained mice to produce reach-to-grasp actions – complex, ethologically relevant behaviors that broadly engage the motor network[13,14,16,17,19,24–28]. The structure of reaching and grasping – a ballistic reach followed by a sensory-guided grasp[29] (**Figure 1a**) – is evolutionarily conserved across species, providing a common framework to study motor control in the

mammalian brain[30–32]. High-resolution movement kinematics were captured as mice learned the task over ten consecutive training days, performing 50 trials per day (**Figure 1b&c**). Trials occurred every 30 seconds, with food pellet presentation paired with a sound cue. Over ten days of training, mice achieved expert success rates (~80-90% success), precise reaction times, and stable trial-to-trial kinematics, including spatial reach trajectory, velocity, grip aperture (hand opening/closing), and supination angle (**Figure 1d**).

After learning, we simultaneously recorded single neurons across five interconnected cerebral and cerebellar motor areas during the production of skilled movements (**Figure 1e**): (1) the frontal cortex (FC) targeting the rostral forelimb area or RFA (8,210 neurons), (2) the primary motor cortex (M1) targeting the caudal forelimb area or CFA (13,362 neurons) – RFA and CFA are the two principal forelimb-related cortical areas[14,15,33,34] – (3) the dorsolateral striatum (DLS), the major basal ganglia area innervated by M1[35,36] (3,312 neurons), (4) the ventral anterior/ventral lateral nuclei of the motor thalamus (mTH) that receive major basal ganglia and cerebellar input[37] (13,494 neurons), and (5) the interposed nucleus of the deep cerebellar nuclei (DCN), a cerebellar output nucleus that projects to the motor cortex via the thalamus and is critical for skilled reaching[17,38–40] (4,670 neurons). Simultaneous recordings provided a single-neuron-resolution multi-area view of neural dynamics during skilled reaching (**Figure 1f**).

Across recorded brain areas, we found both action-modulated neurons (neurons with spiking activity that increased or decreased during action production) and action-informative neurons (neurons whose spiking activity encoded significant information about trial-to-trial movement kinematics). All areas contained both positively and negatively modulated neurons during action production (**Figure 1g**). Positively modulated DLS neurons had the earliest increases in firing rate relative to movement onset of the reach-to-grasp action, while negatively modulated DCN neurons had the earliest decreases (**Figure 1h**). To classify neurons as action-informative or non-informative, we computed Shannon information[41] encoded by each neuron's spiking activity at a range of time lags to future kinematics during reaching, comparing encoded information to a trial-shuffled distribution (**Figure 1i**). Shannon information captures both linear and non-linear encoding of information[42] with significant information indicating that spiking activity is predictive of future kinematics. To capture neurons informative about either gross movements of the forelimb or fine movements of the digits, we computed information about both acceleration and grip aperture. All areas had similar proportions of action-modulated and action-informative neurons (**Figure 1j**). FC and DLS neurons encoded the earliest information about movement – measured as a longer delay between information encoding and upcoming movement (**Figure 1k**).

Selective network coupling-decoupling precedes skilled action.

Given the distributed nature of action-informative neurons across the brain, we examined how these populations may interact to generate skilled action. A simple measure of cross-area interaction is the consistency of spike-timing relationships between neuron pairs across areas – capturing whether one neuron's activity can predict another's or if they act independently. Simultaneous high-yield recordings enable the interpretation of these pairwise relationships by resolving the dominant patterns of interaction across neural populations in each area. By simultaneously recording across five areas, we measured the interaction of 6,658,933 cross-area neuron pairs (1,254,891 FC/M1 pairs, 301,253 FC/DLS pairs, 1,418,721 FC/mTH pairs, 229,530 FC/DCN pairs, 322,068 M1/DLS pairs, 1,731,799 M1/mTH pairs, 384,145 M1/DCN pairs, 404,237 DLS/mTH pairs, 106,358 DLS/DCN pairs, 505,931 mTH/DCN). We computed cross-correlations within action-informative and non-informative cross-area neuron pairs in 500ms time bins (with a 100ms sliding window) over a 20 second window centered on movement onset (**Figure 2a**). Each cross-area neuron pair was assigned a directionality – e.g., DCN to mTH or mTH to DCN – based on the position of the average cross-correlation peak, indicating which area's spikes led or lagged the other. Spike-timing relationships were most dynamic in the ~10s preceding movement onset. We refer to increases/decreases in spike-timing consistency during this pre-movement period as coupling/decoupling.

Two main processes characterized the pre-movement period: coupling between action-informative neurons and decoupling between non-informative neurons. Across brain areas, these dynamics manifested in three distinct patterns: (1) both action-informative and non-informative neurons coupled – e.g., DCN and mTH, (2) only action-informative neurons coupled – e.g., DLS and mTH, and (3) non-informative neurons decoupled while action-informative neurons coupled – e.g., DLS and FC (**Figure 2b**). These interactions were not explained by pre-movement firing rate changes – which primarily occurred after coupling/decoupling and only in specific brain areas (mTH, DLS, and FC; **Supplemental Figure 1a&b**) – nor were they related to positively or negatively modulated neural populations during movement – positively or negatively modulated neurons coupled/decoupled in similar proportions (**Supplemental Figure 1c**). At movement onset, cross-area spike-timing consistency

decreased, consistent with established movement-related desynchronization of neural activity reported across the motor network[43,44]. We determined the significance of coupling and decoupling by measuring the proportion of cross-area neuron pairs (within each direction) that increased or decreased in cross-correlation magnitude preceding movement in each recording session (**Figure 2c**). Across all cross-area pairs, action-informative neurons primarily coupled, while non-informative neurons decoupled. Network maps of significant coupling and decoupling revealed an anterior-posterior gradient, with the most prominent coupling originating from the DCN to cerebral regions (4 of the 6) and decoupling from the FC (4 of the top 4) (**Figure 2d**). This reveals that selective coupling-decoupling dominates the pre-movement period, with each neuron's specific dynamics determined more by its relevance to upcoming behavior than anatomical location.

Network coupling-decoupling predicts skilled action quality.

These rich pre-movement coupling-decoupling dynamics indicate this period may be relevant to prepare for precise action. To test this, we examined whether coupling-decoupling dynamics predict the quality of upcoming action. To measure coupling/decoupling on each trial, we computed the change in average cross-correlation peak during 10s pre-movement across all action-informative pairs that coupled pre-movement or all non-informative pairs that decoupled. Coupling among action-informative pairs was significantly positively correlated with upcoming movement quality on a trial-by-trial basis, across the brain (**Figure 3a&c**). Action quality was quantified as the correlation of each individual trial's kinematics to the mean kinematics of successful actions across that recording session. Conversely, decoupling among non-informative pairs was significantly negatively correlated with upcoming action quality, primarily between anterior brain areas such as the FC, M1, or DLS (**Figure 3b&c**). Combining both measures – the coupling among action-informative pairs and decoupling among non-informative pairs – further strengthened this relationship, especially between anterior areas that exhibited both coupling and decoupling (**Figure 3c**). These relationships were robust beyond our specific criteria for action-informative or non-informative neurons – averaging across all coupled or decoupled cross-area pairs, rather than only action-informative and non-informative ones, produced statistically identical results (data not shown). Additionally, relationships between action quality and pre-movement firing-rate changes were substantially weaker (**Supplemental Figure 1d**). These results suggest that precise actions result from the selective engagement of action-relevant interactions and disengagement of irrelevant ones before movement begins.

Early trial onset disrupts network coupling-decoupling and impairs skilled action

To test the necessity of these dynamics to produce skilled actions, we varied the inter-trial interval. We reasoned that starting trials before the emergence of typical coupling-decoupling dynamics would reveal whether these processes are necessary to consistently produce high quality skilled actions. After training mice with a consistent 30s inter-trial interval, we started a subset of trials at 20s (early), 30s (regular), or 40s (late) intervals (**Figure 3d**). Reaction times remained stable across conditions (early: 113.9 ± 17.7ms; regular: 120.0 ± 13.6ms; late: 96.4 ± 6.5ms; early/regular: $t(1031)=-0.21$, $P=0.836$; early/late: $t(402)=0.96$, $P=0.340$; regular/late: $t(1047)=0.86$, $P=0.390$, two-sample t-tests). Early cue trials showed both significantly reduced action-informative coupling and non-informative decoupling compared to regular and late cue trials (**Figure 3e&f**). Consistent with the idea that coupling-decoupling dynamics are necessary to produce high quality actions, movements were significantly more variable during early cue trials compared to regular and late cue trials (**Figure 3g&h**).

Multiplexed oscillations mirror network coupling-decoupling.

Given the central role of oscillatory coherence in dynamically gating inter-area communication[45,46], we examined whether these neuron-pair interactions were reflected in population-level oscillations. We identified pre-movement cross-area oscillatory changes by computing local field potential (LFP) coherence across low frequencies (1-30Hz) between all areas during the 10s preceding movement onset using 500ms time bins and a 100ms sliding window (**Figure 4a**). Two frequency bands showed clear pre-movement changes: an emerging 2-8Hz rhythm, most prominent between posterior areas such as DCN and mTH, and a decreasing 10-18Hz rhythm, most prominent between anterior areas such as FC and M1 (**Figure 4a&b**). Network maps of significant increases and decreases in coherence revealed an anterior-posterior gradient mirroring coupling-decoupling patterns (**Figure 4b**). Pre-movement changes in LFP power exhibited a similar organization, with increased 2-8Hz power localized to DCN and decreased 10-18Hz power observed across cerebral regions (**Supplemental Figure 2a&b**)

LFP coherence and coupling-decoupling were also closely aligned on a trial-by-trial basis. We measured 4Hz LFP coherence during the 5s preceding movement onset on each trial between mTH and DCN (**Figure 4c**; the

area pair with the largest 2-8Hz increase; 4Hz was the peak increase) and 12Hz LFP coherence between FC and M1 (**Figure 4d**; the area pair with the largest 10-18Hz decrease; 12Hz was the peak decrease), and compared it to the average cross-correlation peak during the 5s preceding movement onset on each trial across all action-informative pairs that coupled pre-movement or all non-informative pairs that decoupled. Across the brain, 4Hz coherence was positively correlated with action-informative coupling (**Figure 4c**). In contrast, 12Hz coherence showed a bidirectional relationship – negatively correlated with action-informative coupling but positively correlated with non-informative decoupling – most prominently between anterior regions (FC, M1, DLS; **Figure 4d**). This bidirectional relationship parallels the unique patterns of both coupling and decoupling observed in anterior areas (**Figure 2d**). The relationship between a decrease in 12Hz coherence and an increase in coupling between action-informative neurons is consistent with work in primates, which proposes that beta oscillations prevent the initiation of specific movement-generating patterns[47]. Lastly, we examined whether the emerging 4Hz rhythm entrained neural spiking. Action-informative neurons were preferentially phase-locked to 4Hz LFP signals pre-movement (**Figure 4e&f**), suggesting that the consistency of cross-area spike-timing relationships may be supported by an emerging low-frequency cross-area oscillation.

Pupil dynamics reflect network coupling-decoupling.

The timescale of these network dynamics would be consistent with a neuromodulator influence. To explore this possibility, we measured changes in pupil size. Pupil size significantly increased pre-movement (**Supplemental Figure 3a**). On a trial-by-trial basis, pupil size was significantly positively correlated with 4Hz LFP coherence and negatively correlated with 12Hz coherence (**Supplemental Figure 3b**). Pupil size was also significantly positively correlated with action-informative coupling across the brain and non-informative decoupling in anterior brain regions (**Supplemental Figure 3c**). This identifies pupil dynamics as a robust non-invasive biomarker of large-scale network coupling-decoupling, suggesting a potential role for neuromodulators such as acetylcholine and norepinephrine that are closely linked to pupil dynamics and have established roles in regulating neural synchrony[48].

External modulation of cross-area dynamics bidirectionally impacts skilled action quality.

The identified relationships between population-level oscillatory coherence and neuron-level coupling-decoupling revealed an opportunity for causal intervention. Pre-movement 4Hz LFP coherence was strongest between DCN and mTH and correlated with brain-wide coupling among action-informative neurons, suggesting that this rhythm enables inputs from DCN to reach mTH at an optimal phase, consistent with established theories of oscillatory gating of inter-area communication[21–23,48]. If so, altering the relative phase between DCN and mTH should enhance or disrupt this cross-area coordination and, in turn, action quality. To test this, we optogenetically modulated cerebellar and cortico-thalamic neural populations in VGAT-ChR2 expressing mice (**Figure 5a**). Two optical fibers targeted lobule simplex of the cerebellar cortex, the region projecting to the interposed nucleus of the DCN, and M1 – while we recorded neural activity in the DCN and mTH. On each trial, 4s of 4Hz sinusoidal light stimulation was provided to both regions, ending 500ms prior to trial cue (**Figure 5a**). The phase difference between cerebellar and cortical stimulation was systematically shifted across 16 trial types, allowing us to sample a full cycle of relative phase differences (**Figure 5a**). Both action-informative and non-informative mTH and DCN neurons were entrained to cortical and cerebellar stimulation, respectively (**Figure 5b**). This non-specificity of optogenetic manipulations (entraining both action-informative and non-informative neurons) matched the coupling dynamics of these areas, as both action-informative and non-informative neurons typically coupled between DCN, mTH, and M1 (**Figure 2c&d**).

Consistent with the robust entrainment of DCN and mTH neural populations, we were able to drive a range of spike-timing relationships across trial types that systematically varied in similarity to the physiological spike-timing relationship measured between DCN and mTH on successful non-laser trials (**Figure 5c**). If this rhythm supports cross-area spike-timing relationships that enable precise action production, trial types that drive 4Hz coherence at this physiological phase difference should enhance coupling and improve the consistency of movements. In contrast, driving 4Hz coherence at non-physiological phase differences should disrupt movement quality. We found this exact bidirectional impact on movement quality, with cross-area spike-timing relationships that corresponded to the dynamics on successful non-laser trials improving movement consistency and success rate, while driving atypical dynamics disrupted behavior (**Figure 5d**). This highlights the importance of cross-area dynamics prior to skilled action and identifies pre-movement cross-area oscillations as tractable targets for intervention.

Discussion

We found skilled reach-to-grasp actions are preceded by a period of rich cross-area interactions dominated by coupling among action-informative neurons – defined as increased consistency of spike-timing relationships – and decoupling among non-informative neurons. The trial-by-trial magnitude of this coupling-decoupling predicted the quality of upcoming actions. Two oscillations mirrored these dynamics: an emerging low-frequency (2-8Hz) coherence associated with coupling and a decreasing higher frequency (10-18Hz) coherence associated with decoupling. These processes were distributed along a posterior–anterior gradient, with coupling and low-frequency coherence biased posterior (e.g., DCN/mTH) and decoupling and higher-frequency coherence biased anterior (e.g., FC/M1). We optogenetically manipulated cross-area oscillatory dynamics to establish that precise cross-area dynamics are required for skilled action. Together, our results reveal a process by which distributed neurons relevant to a specific behavior are selectively coordinated to ensure precision and consistency.

Skilled motor control is fundamentally distributed.

Widespread neural modulation across the brain has been observed during movement[7–10]. Our work underscores the importance of a cross-area perspective for understanding how the motor network controls skilled actions. The processes we identified were distributed rather than confined to any specific area, with each individual neuron's interactions more closely resembling those of spatially distant neurons with similar behavioral relevance rather than nearby neighbors without. Our work highlights that the neural correlates of motor control identified within individual areas can only be fully interpreted in the context of cross-area coordination. Just as studying one quadrant of the heart would not explain how it circulates blood, examining a single brain region provides only a limited view of how the brain controls skilled movements.

Isolating behaviorally relevant dynamics reveals complex cross-area coordination.

Understanding how distributed networks contribute to motor control requires isolating behaviorally relevant interactions from global dynamics. We show that distinct neural populations between the same two areas can simultaneously exhibit opposing forms of interaction – coupling among action-informative neurons and decoupling among non-informative neurons. This is consistent with work demonstrating that task-relevant cross-area dynamics can substantially differ from overall, non-specific measures of neural interaction[21–23,49]. These results emphasize the need for single-neuron-resolution multi-area studies to distinguish diverse forms of interactions that coexist within distributed neural populations. Linking such single-neuron interaction dynamics to emerging analytical tools for identifying behaviorally relevant subspaces[50,51] will be essential for understanding how distributed networks work together to control complex movements.

Motor control integrates general principles of network selection.

Multiple mechanisms proposed for network selection appear to cooperate in motor control. First, control hubs such as the prefrontal cortex and thalamus can align widespread activity with task goals[54,55]. Consistent with this idea, we found control hub-like organization in the motor network: anterior areas like FC both coupled and decoupled with other areas – consistent with task-relevant routing of neural activity – while posterior areas like DCN predominantly coupled with other areas, suggesting a central coordinating role. Second, oscillatory coherence can gate cross-area communication by determining whether inputs arrive in or out of phase[52–54]. We found both increases and decreases in coherence that paralleled neuron-level coupling-decoupling, linking oscillations to neural communication consistent with this proposed mechanism. We also demonstrated that optogenetic manipulations that altered whether DCN inputs arrived in or out of phase with mTH bidirectionally impacted action quality, emphasizing the causal importance of oscillatory gating for behavior. Third, behavioral state, including attention and arousal, can broadly influence effective connectivity[48,52]. We found trial-by-trial pupil dynamics tracked both coupling-decoupling and coherence, suggesting a neuromodulator influence on network interactions. This work indicates that control hubs, oscillatory coherence, and state-dependent modulation jointly shape how distributed motor networks coordinate to produce precise and consistent action.

Motor preparation as a cross-area process.

Preparatory neural activity has been extensively studied in motor control, with classic work linking firing-rate modulations that precede movement in motor cortex to upcoming parameters such as direction and speed[53–55]. Preparatory rate changes have also been reported in connected areas of the motor networks, including

thalamus[56,57], and basal ganglia[58]. Consistent with this work, we found pre-movement rate changes in several areas (DLS, mTH, FC; **supplemental figure 1**). We also find timing-based changes in the consistency of spike-timing relationships between cross-area neuron pairs, and that these changes often precede rate changes and are better predictors of upcoming action quality. This suggests motor preparation is a distributed process expressed in both cross-area spike-timing and rate changes. Timing-based preparatory dynamics have been described in the motor cortex, where spike synchrony can mark internal events such as stimulus expectancy without accompanying rate changes[59,60]. Our results extend this to a network-level process. A notable difference in our work is the long preparatory window (~10s), likely reflecting the consistent 30s inter-trial-interval. This indicates that the nervous system can utilize this stable temporal scaffold to optimally prepare distributed networks to produce a precise action.

Pre-movement dynamics as a therapeutic window.

The rich cross-area dynamics we observe before movement – when sensory and motor drive are relatively low – offer a practical opportunity to measure coordination (e.g., via pupil or LFP) and to intervene when coordination is atypical. Our optogenetic phase-alignment manipulation provides proof-of-principle of a tractable control parameter for shaping motor network interactions that underlie motor control. Conditions characterized by atypical network connectivity[61] may particularly benefit from interventions that restore precise cross-area neural dynamics.

Limitations and future directions.

We identify a principle by which a distributed network is selected to produce specific behavior. Whether this principle generalizes to other behaviors and how different task-relevant networks flexibly reconfigure remain open questions. Our recordings spanned five motor areas but did not cover other key areas such as somatosensory cortex and brainstem that may be involved in motor and other behaviors. As our optogenetic entrainment recruited mixed populations, the advancement of interventional tools to target select neural populations will refine causal testing.

Acknowledgements.

This study was supported by grants from the NICHD/NIH T32HD040127 (S.M.L.), NINDS/NIH F32NS131217 (S.M.L.), NINDS/NIH R01NS118030-01A1 (A.W.H.). The authors thank members of the Hantman laboratory for helpful comments, guidance, and discussion about the manuscript. The authors thank Jeremy Cohen for technical assistance and Scott Albert and Trisha Vaidyanathan for feedback on the manuscript.

Author contributions.

S.M.L., J-Z.G., and A.W.H. conceptualized the project and designed the experiments. S.M.L., S.A., and J-Z.G. performed surgeries and collected behavioral and neural data. S.M.L. analyzed the data. S.M.L. wrote the manuscript with input from A.W.H. A.W.H. and J-Z.G. supervised the project.

Competing interests.

The authors declare no competing interests.

Materials & Correspondence.

All inquiries can be sent to A.W.H. (adam_hantman@unc.edu) and S.M.L. (stefan.lemke@unc.edu). All the source data and code used in this work will be publicly available upon final publication.

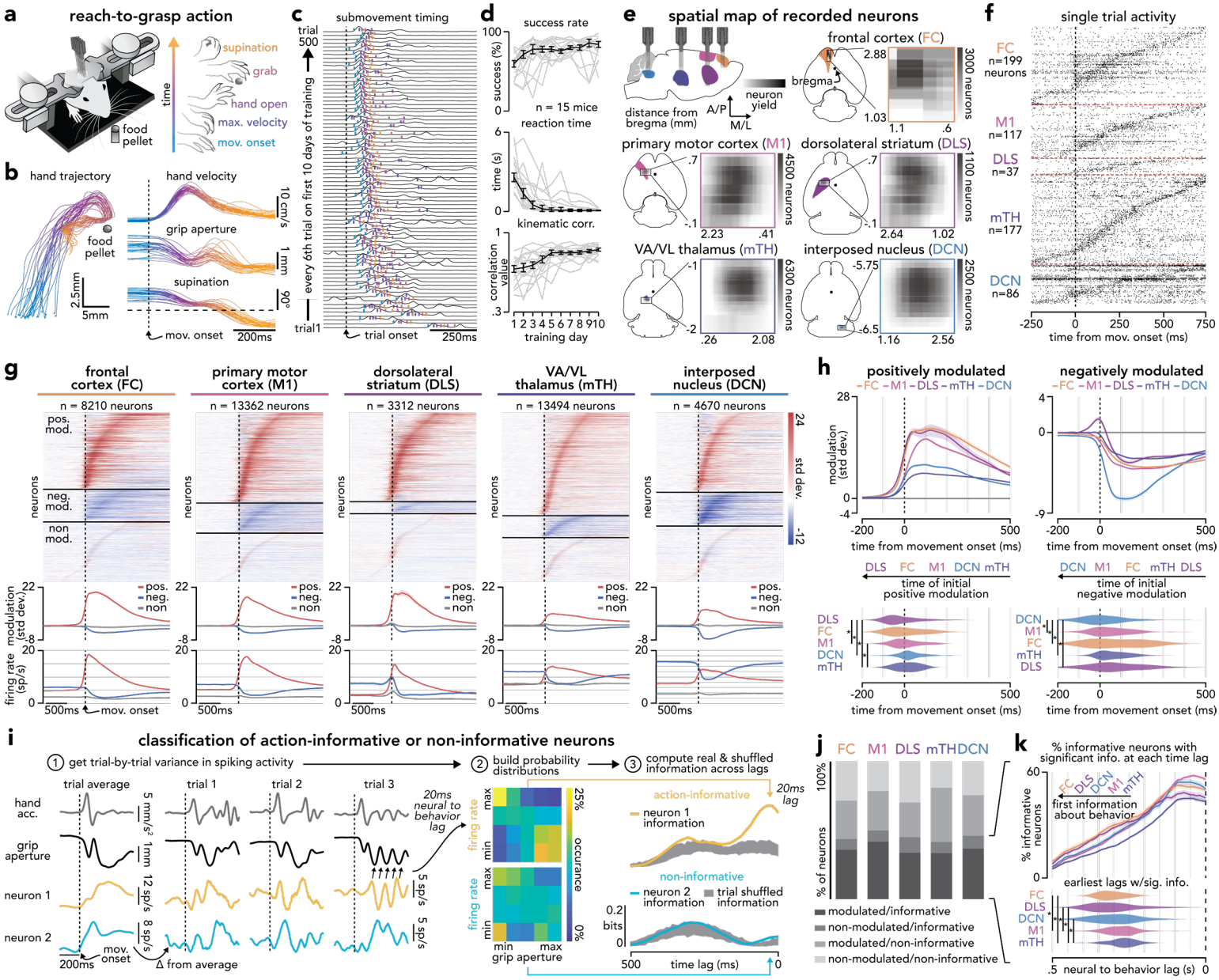

Figure 1: Action information and modulation are widely distributed across the brain.

(a) Schematic of the reach-to-grasp action and its sub-movements.
(b) Example kinematics from a skilled reach-to-grasp action.
(c) Evolution of sub-movement timing during 10 days of training (50 trials/day) in an example animal (every 6th trial plotted).
(d) Learning curves across 10 days of training (50 trials/day) for individual animals (thin lines) and mean ± SEM across animals (bold; n = 15 mice).
(e) Schematic of single-neuron recording yield for each brain area, showing neuron yield across spatial locations.
(f) Simultaneously recorded neural activity across areas during an example reach-to-grasp action.
(g) Cascade plots of trial-averaged single-neuron modulation across animals in each area (top) and mean modulation and firing rate for positively, negatively, and non-modulated neurons during action production (bottom; width of lines denotes mean±SEM across sessions).
(h) Comparison of modulation timing across positively/negatively modulated neurons in each area (width of lines denotes mean±SEM across sessions; asterisk denotes significance at $P<0.05$, Bonferroni-corrected, Wilcoxon rank sum test; positively-modulated: DLS/FC: $P=0.11$, DLS/M1: $P=0.002$, DLS/mTH: $P<0.001$, DLS/DCN: $P<0.001$, FC/M1: $P=0.71$, FC/mTH: $P=0.03$, FC/DCN; $P=0.27$, M1/mTH: $P<0.001$, M1/DCN: $P=0.12$, mTH/DCN: $P=0.15$; negatively-modulated: DCN/DLS: $P<0.001$, DCN/M1: $P=0.007$, DCN/mTH: $P<0.001$, DCN/FC: $P<0.001$, DLS/M1: $P=0.35$, DLS/mTH: $P=0.14$, DLS/FC: $P=0.10$, M1/mTH: $P=0.96$, M1/FC: $P=0.93$, mTH/FC: $P=0.59$; FC: $n=39$ sessions (6 mice), M1: $n=138$ (17), DLS: $n=117$-129 (17), mTH: $n=95$ (12), DCN: $n=112$-113 (16).
(i) Schematic of action-informative and non-informative neuron classification using Shannon information.
(j) Proportion of action-modulated and action-informative neurons in each area.

(k) Percent of action-informative neurons with significant information at each behavior-to-neural time delay (top; width of lines denotes mean±SEM across sessions) and distribution of earliest time lags with significant information for each recording session (bottom; asterisk denotes significance at $P<0.05$, Bonferroni-corrected, Wilcoxon rank sum test; FC/DLS: $P=0.55$, FC/DCN: $P=0.45$, FC/M1: $P<0.001$, FC/mTH: $P<0.001$, DLS/DCN: $P=0.2$, DLS/M1: $P<0.001$, DLS/mTH: $P<0.001$, DCN/M1: $P=0.02$, DCN/mTH: $P<0.001$, M1/mTH: $P=0.09$; FC: $n=39$ sessions (6 mice), M1: $n=138$ (17), DLS: $n=128$ (17), mTH: $n=95$ (12), DCN: $n=114$ (16).

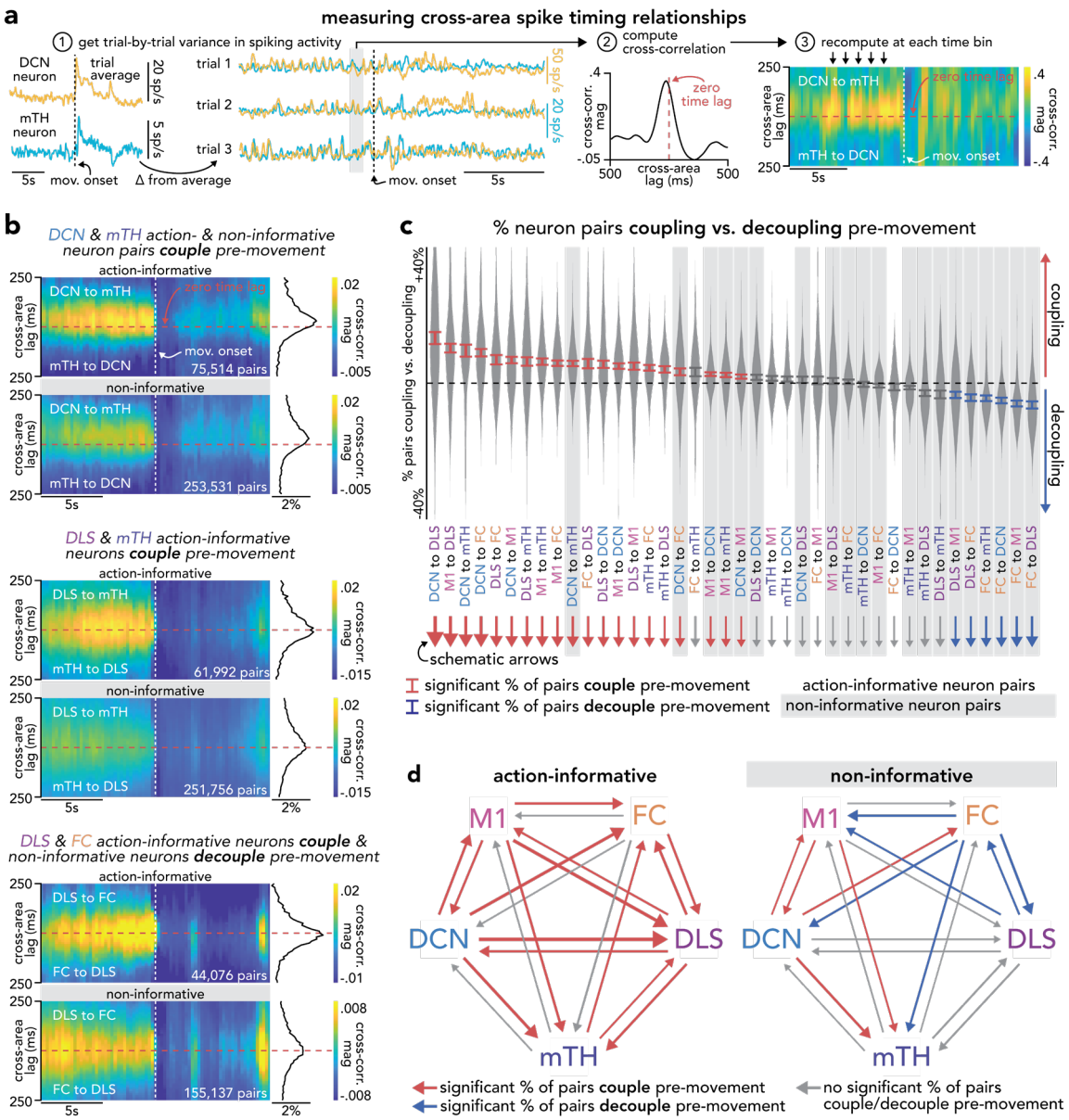

Figure 2: Selective network coupling-decoupling precedes skilled action.

(a) Schematic of cross-correlation computation between cross-area neuron pairs.

(b) Cross-correlation magnitude over time relative to movement onset for action-informative (top) and non-informative (bottom) cross-area neuron pairs for three pairs of brain areas. Heatmaps show correlation magnitude across time and time lags; associated histograms show the distribution of peak cross-correlation lags. Distinct coupling-decoupling dynamics are observed across brain areas and action-informative or non-informative neurons.

(c) Difference between the percentage of cross-area neuron pairs that significantly increased (coupled) vs. decreased (decoupled) cross-correlation magnitude during the 10s preceding movement. Red and blue bars indicate values significantly above or below zero, shaded bars indicate non-informative neuron pairs ($P < 0.05$, Bonferroni-corrected, one-sample *t*-test). Action-informative pairs (ordered by positive-to-negative difference): DCN to DLS: $t(108)=7.52$, $P<0.001$, M1 to DLS: $t(125)=8.44$, $P<0.001$, DCN to mTH: $t(83)=8.85$, $P<0.001$, DCN to FC: $t(45)=5.44$, $P<0.001$, DLS to FC: $t(50)=5.01$, $P<0.001$, DCN to M1: $t(112)=7.58$, $P<0.001$, DLS to mTH: $t(91)=5.50$, $P<0.001$, M1 to mTH: $t(92)=8.28$, $P<0.001$, M1 to FC: $t(53)=6.69$, $P<0.001$, FC to DLS: $t(50)=4.20$, $P<0.001$, DLS to DCN: $t(108)=5.56$, $P<0.001$, M1 to DCN: $t(112)=6.53$, $P<0.001$, DLS to M1: $t(125)=4.79$, $P<0.001$, mTH to FC: $t(50)=5.48$, $P<0.001$, mTH to DLS: $t(91)=3.84$, $P<0.001$, FC to mTH: $t(50)=2.68$, $P=0.009$, mTH to M1: $t(92)=2.61$, $P=0.01$, mTH to DCN: $t(83)=1.79$, $P=0.08$, FC to M1: $t(53)=1.14$, $P=0.26$, FC to DCN: $t(45)=-1.11$, $p=0.27$; non-informative: DCN to mTH: $t(83)=8.22$, $P<0.001$; DCN to FC: $t(45)=4.32$, $P<0.001$; M1 to DCN: $t(112)=5.76$, $P<0.001$; M1 to mTH: $t(92)=4.83$, $P<0.001$; DCN to M1: $t(112)=3.56$, $P<0.001$; DLS to DCN: $t(108)=2.33$, $P=0.02$; DCN to DLS: $t(108)=0.82$, $P=0.41$; M1 to DLS: $t(126)=0.77$, $P=0.44$; mTH to FC: $t(50)=0.69$, $P=0.50$; mTH to DCN: $t(83)=-0.58$, $P=0.57$; M1 to FC: $t(53)=-0.45$, $P=0.65$; mTH to M1: $t(92)=-1.64$, $P=0.10$; mTH to DLS: $t(91)=-3.29$, $P=0.001$; DLS to mTH: $t(91)=-2.72$, $P=0.007$; DLS

to M1: $t(126)=-3.95$, $P<0.001$; DLS to FC: $t(50)=-4.34$, $P<0.001$; FC to mTH: $t(50)=-5.28$, $P<0.001$; FC to DCN: $t(45)=-6.10$, $P<0.001$; FC to M1: $t(53)=-6.92$, $P<0.001$; FC to DLS: $t(50)=-6.11$, $P<0.001$; FC: n=46–54 sessions, M1: n=54–127 sessions, DLS: n=51–127 sessions, mTH: n=51–93 sessions, DCN: n=46–113 sessions.

(d) Network diagrams summarizing significant changes in percentage of cross-area neuron pairs that couple and decouple in the 10s preceding movement. Arrows indicate direction and width reflects magnitude of change. Red = significant increase; blue = significant decrease. Separate diagrams shown for action-informative and non-informative neuron pairs.

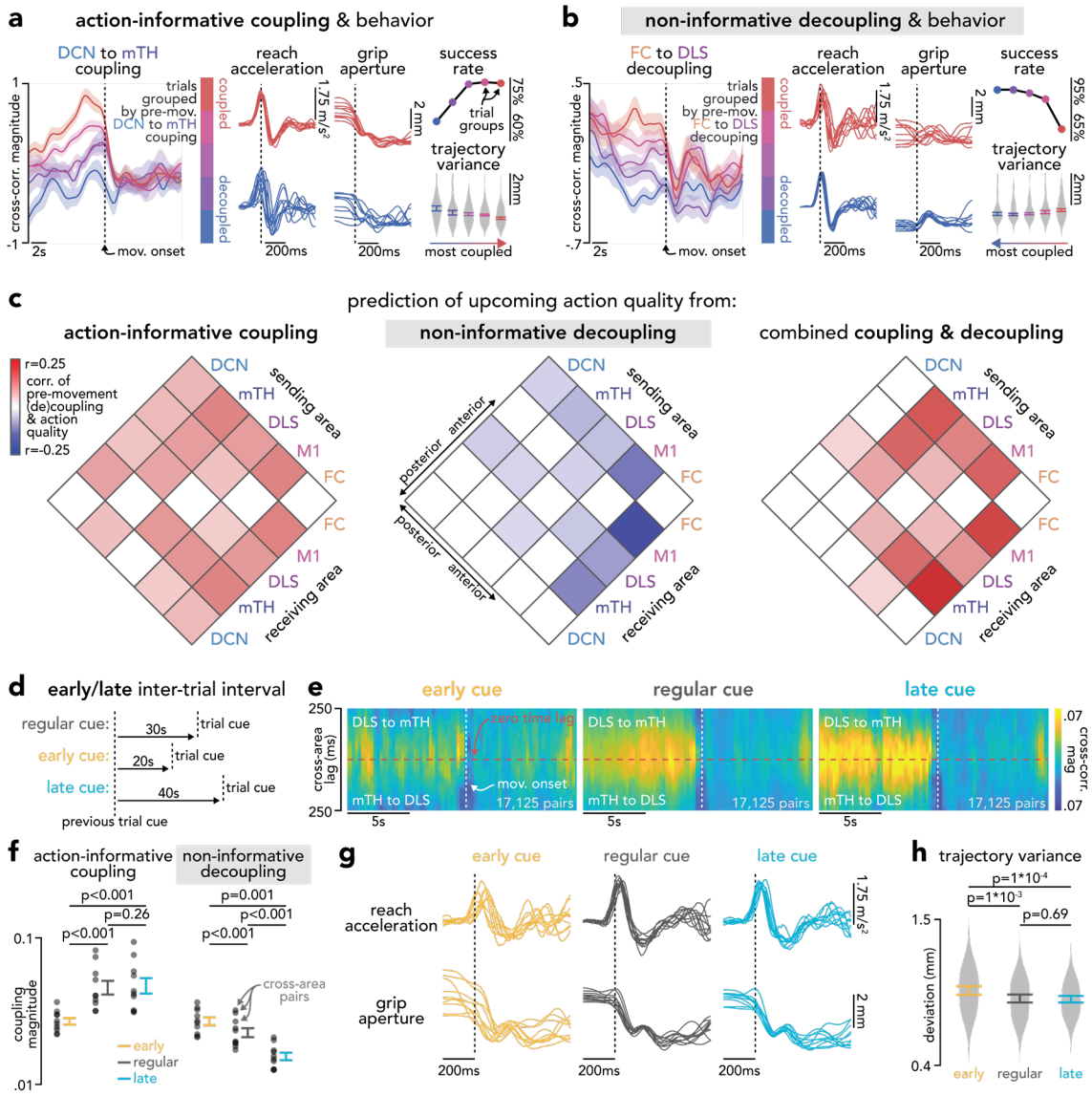

Figure 3: Network coupling-decoupling predicts skilled action quality.

(a) Increases in pre-movement action-informative coupling are correlated with increased action quality. Trials grouped by pre-movement coupling magnitude between action-informative DCN-to-mTH neuron pairs (left; line width denotes mean±SEM across trials in each group, n=268 trials in 5 subgroups), example reach acceleration and grip aperture for lowest and highest coupling groups (middle), and success rate and trajectory variance across groups (right).

(b) Same as **(a)** for non-informative FC-to-M1 neuron pairs (n=326 trials in 5 subgroups).

(c) Matrix of correlations linking trial-by-trial action quality (kinematic correlation) to pre-movement changes in either (1) coupling within action-informative cross-area neuron pairs (left), (2) decoupling within non-informative cross-area neuron pairs (middle), or (3) the difference in magnitude of coupling in action-informative pairs and decoupling in non-informative pairs (color denotes significance at $P<0.05$, Bonferroni-corrected, Spearman correlation; action-informative coupling: M1 to DLS: $r=0.07$, $P<0.001$; DLS to M1: $r=0.06$, $P<0.001$; M1 to DCN: $r=0.07$, $P<0.001$; DCN to M1: $r=0.08$, $P<0.001$; M1 to mTH: $r=0.12$, $P<0.001$; mTH to M1: $r=0.15$, $P<0.001$; M1 to FC: $r=0.15$, $P<0.001$; FC to M1: $r=0.15$, $P<0.001$; DLS to DCN: $r=0.04$, $P=0.003$; DCN to DLS: $r=0.07$, $P<0.001$; DLS to mTH: $r=0.13$, $P<0.001$; mTH to DLS: $r=0.11$, $P<0.001$; DLS to FC: $r=0.12$, $P<0.001$; FC to DLS: $r=0.12$, $P<0.001$; DCN to mTH: $r=0.11$, $P<0.001$; mTH to DCN: $r=0.08$, $P<0.001$; DCN to FC: $r=0.09$, $P<0.001$; FC to DCN: $r=0.09$, $P<0.001$; mTH to FC: $r=0.15$, $P<0.001$; FC to mTH: $r=0.15$, $P<0.001$; non-informative decoupling: M1 to DLS: $r=-0.07$, $P<0.001$; DLS to M1: $r=-0.06$, $P<0.001$; M1 to DCN: $r=-0.01$, $P=0.52$; DCN to M1: $r=-0.03$, $P=0.017$; M1 to mTH: $r=-0.02$, $P=0.043$; mTH to M1: $r=-0.03$, $P=0.005$; M1 to FC: $r=-0.16$, $P<0.001$; FC to M1: $r=-0.24$, $P<0.001$; DLS to DCN: $r=-0.02$, $P=0.037$; DCN to DLS: $r=-0.06$, $P<0.001$; DLS to mTH: $r=-0.05$, $P<0.001$; mTH to DLS: $r=-0.05$, $P=0.001$; DLS to FC: $r=-0.08$, $P<0.001$; FC to DLS: $r=-0.12$, $P<0.001$; DCN to mTH: $r=-0.02$, $P=0.17$; mTH to DCN: $r=-0.00$, $P=0.97$; DCN to FC: $r=-0.05$, $P=0.002$; FC to DCN: $r=-0.05$, $P=0.003$; mTH to FC: $r=-0.09$, $P<0.001$; FC to mTH: $r=-0.09$, $P<0.001$; combined coupling and decoupling: M1 to DLS: $r=0.08$, $P<0.001$; DLS to M1: $r=0.09$, $P<0.001$; M1 to DCN: $r=0.05$, $P<0.001$; DCN to M1: $r=0.03$, $P=0.006$; M1 to

mTH: r=0.18, P<0.001; mTH to M1: r=0.18, P<0.001; M1 to FC: r=0.19, P<0.001; FC to M1: r=0.22, P<0.001; DLS to DCN: r=0.01, P=0.57; DCN to DLS: r=0.05, P<0.001; DLS to mTH: r=0.09, P<0.001; mTH to DLS: r=0.11, P<0.001; DLS to FC: r=0.15, P<0.001; FC to DLS: r=0.13, P<0.001; DCN to mTH: r=0.02, P=0.14; mTH to DCN: r=0.00, P=0.93; DCN to FC: r=0.01, P=0.51; FC to DCN: r=0.04, P=0.06; mTH to FC: r=0.20, P<0.001; FC to mTH: r=-0.26, P<0.001).

(d) Schematic of inter-trial interval manipulation.

(e) Cross-correlation magnitude over time relative to movement onset for action-informative DCN and mTH neuron pairs across cross-area time lags, during early, regular, and late cue trials.

(f) Comparison of average coupling magnitude across all cross-area pairs during early, regular, and late cue trials (action-informative: early/regular: t(18)=-3.4, P=0.003, early/late: t(18)=-3.5, P=0.003, regular/late: t(18)=1.4, P=0.17; non-informative: early/regular: t(18)=-1.4, P=0.17; early/late: t(18)=-0.6, P=0.57; regular/late: t(18)=0.4, P=0.72, two-sample t-test, n = 10 area pairs).

(g) Reach acceleration and grip aperture during example early, regular, and late cue trials.

(h) Comparison of trajectory variance during early, regular, and late cue trials (early/regular: t(17)=3.84, P=0.001; early/late: t(17)=4.93, P<0.001; regular/late: t(17)=0.40, P=0.692, paired-sample t-test, n = 18 sessions).

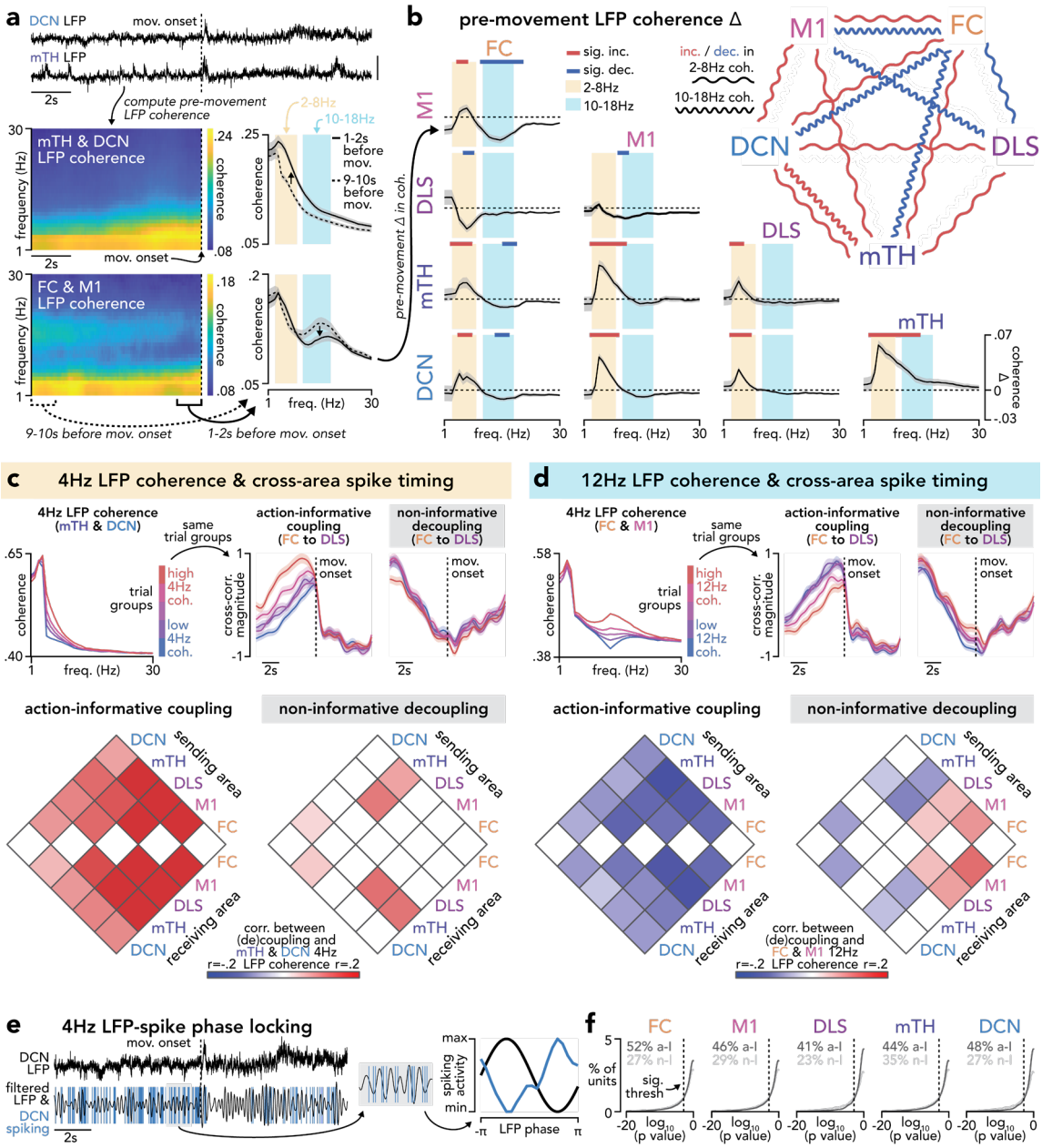

Figure 4: Multiplexed oscillations mirror coupling-decoupling.

(a) Example computation of pre-movement LFP coherence.

(b) LFP coherence spectra showing changes in cross-area coherence during 10s pre-movement (left). Yellow and blue bars indicate the 2–8 Hz and 10–18 Hz frequency ranges, respectively. Red and blue significance bars above each spectrum indicate frequencies with significant increases or decreases, respectively ($P < 0.05$, Wilcoxon signed-rank test, Bonferroni-corrected). The network schematic (top right) summarizes significant increases (red) or decreases (blue) in coherence within 2-8 Hz (low-frequency squiggly lines) or 10-18 Hz (high-frequency squiggly lines).

(c) Relationship between pre-movement mTH and DCN 4Hz LFP coherence and coupling-decoupling across all area pairs. Top: mTH and DCN LFP coherence spectra for trial groups separated by 4Hz coherence magnitude, and FC to DLS action-informative coupling and non-informative decoupling for the same trial groups. Bottom: Matrix of correlations between pre-movement mTH and DCN 4Hz LFP coherence and action-informative coupling (left) or non-informative decoupling (right) for all pairs of sending/receiving areas (color denotes significance at $P<0.05$, Bonferroni-corrected, Spearman correlation; action-informative: M1 to DLS: $r=0.21$, $P<0.001$; DLS to M1: $r=0.22$, $P<0.001$; M1 to DCN: $r=0.12$, $P<0.001$; DCN to M1: $r=0.14$, $P<0.001$; M1 to mTH: $r=0.23$, $P<0.001$; mTH to M1: $r=0.16$, $P<0.001$; M1 to FC: $r=0.25$, $P<0.001$; FC to M1: $r=0.30$, $P<0.001$; DLS to DCN: $r=0.10$, $P<0.001$; DCN to DLS: $r=0.12$, $P<0.001$; DLS to mTH: $r=0.17$, $P<0.001$; mTH to DLS: $r=0.15$, $P<0.001$; DLS to FC: $r=0.21$, $P<0.001$; FC to DLS: $r=0.25$, $P<0.001$; DCN to mTH: $r=0.10$, $P<0.001$; mTH to DCN: $r=0.07$, $P<0.001$; DCN to FC: $r=0.09$, $P<0.001$; FC to DCN: $r=0.11$, $P<0.001$; mTH to FC: $r=0.22$, $P<0.001$; FC to mTH: $r=0.27$, $P<0.001$; non-informative: M1 to DLS: $r=-0.00$, $P=0.87$; DLS to M1: $r=-0.02$, $P=0.21$; M1 to DCN: $r=0.02$, $P=0.07$; DCN to M1: $r=0.01$, $P=0.26$; M1 to mTH: $r=0.14$, $P<0.001$; mTH to M1: $r=0.13$,

P<0.001; M1 to FC: *r*=0.05, *P*=0.004; FC to M1: *r*=0.02, *P*=0.30; DLS to DCN: *r*=0.02, *P*=0.13; DCN to DLS: *r*=0.02, *P*=0.24; DLS to mTH: *r*=0.04, *P*=0.007; mTH to DLS: *r*=0.02, *P*=0.11; DLS to FC: *r*=-0.03, *P*=0.15; FC to DLS: *r*=-0.03, *P*=0.14; DCN to mTH: *r*=0.04, *P*=0.002; mTH to DCN: *r*=0.05, *P*<0.001; DCN to FC: *r*=-0.03, *P*=0.06; FC to DCN: *r*=-0.03, *P*=0.08; mTH to FC: *r*=0.09, *P*<0.001; FC to mTH: *r*=0.13, *P*<0.001).

(d) Relationship between pre-movement FC and M1 12Hz LFP coherence and coupling-decoupling across all area pairs. Top: FC and M1 LFP coherence spectra for trial groups separated by 12Hz coherence magnitude, and FC to DLS action-informative coupling and non-informative decoupling for the same trial groups. Bottom: Matrix of correlations between pre-movement FC and M1 12Hz LFP coherence and action-informative coupling (left) or non-informative decoupling (right) for all pairs of sending/receiving areas (color denotes significance at *P*<0.05, Bonferroni-corrected; action-informative: M1 to DLS: *r*=-0.17, *P*<0.001; DLS to M1: *r*=-0.13, *P*<0.001; M1 to DCN: *r*=-0.09, *P*<0.001; DCN to M1: *r*=-0.08, *P*<0.001; M1 to mTH: *r*=-0.11, *P*<0.001; mTH to M1: *r*=-0.14, *P*<0.001; M1 to FC: *r*=-0.14, *P*<0.001; FC to M1: *r*=-0.14, *P*<0.001; DLS to DCN: *r*=-0.06, *P*=0.002; DCN to DLS: *r*=-0.10, *P*<0.001; DLS to mTH: *r*=-0.13, *P*<0.001; mTH to DLS: *r*=-0.15, *P*<0.001; DLS to FC: *r*=-0.17, *P*<0.001; FC to DLS: *r*=-0.18, *P*<0.001; DCN to mTH: *r*=-0.08, *P*<0.001; mTH to DCN: *r*=-0.10, *P*<0.001; DCN to FC: *r*=-0.11, *P*<0.001; FC to DCN: *r*=-0.10, *P*<0.001; mTH to FC: *r*=-0.18, *P*<0.001; FC to mTH: *r*=-0.12, *P*<0.001; non-informative: M1 to DLS: *r*=0.06, *P*<0.001; DLS to M1: *r*=0.06, *P*<0.001; M1 to DCN: *r*=-0.06, *P*<0.001; DCN to M1: *r*=-0.06, *P*=0.002; M1 to mTH: *r*=-0.08, *P*<0.001; mTH to M1: *r*=-0.12, *P*<0.001; M1 to FC: *r*=0.10, *P*<0.001; FC to M1: *r*=0.14, *P*<0.001; DLS to DCN: *r*=-0.00, *P*=0.85; DCN to DLS: *r*=-0.05, *P*=0.004; DLS to mTH: *r*=0.02, *P*=0.24; mTH to DLS: *r*=-0.02, *P*=0.32; DLS to FC: *r*=0.06, *P*<0.001; FC to DLS: *r*=0.09, *P*<0.001; DCN to mTH: *r*=-0.09, *P*<0.001; mTH to DCN: *r*=-0.09, *P*<0.001; DCN to FC: *r*=-0.05, *P*=0.009; FC to DCN: *r*=-0.02, *P*=0.24; mTH to FC: *r*=-0.10, *P*<0.001; FC to mTH: *r*=-0.03, *P*=0.11).

(e) Example raw LFP from DCN during a single reaching trial (top left) and corresponding 4Hz-filtered LFP with overlaid spike times from an example DCN neuron (bottom left). Polar histogram showing the distribution of spike phases for the same neuron during the pre-movement period (right).

(f) Percentage of units significantly phase-locked to 4Hz LFP oscillations across areas (Rayleigh test for circular non-uniformity; *P* < 0.05). Plots show the distribution of log-transformed p-values for all recorded units. Dashed line indicates significance threshold. Summary statistics above each plot show the percentage of significantly phase-locked action-informative (a-I) and non-informative (n-I) units.

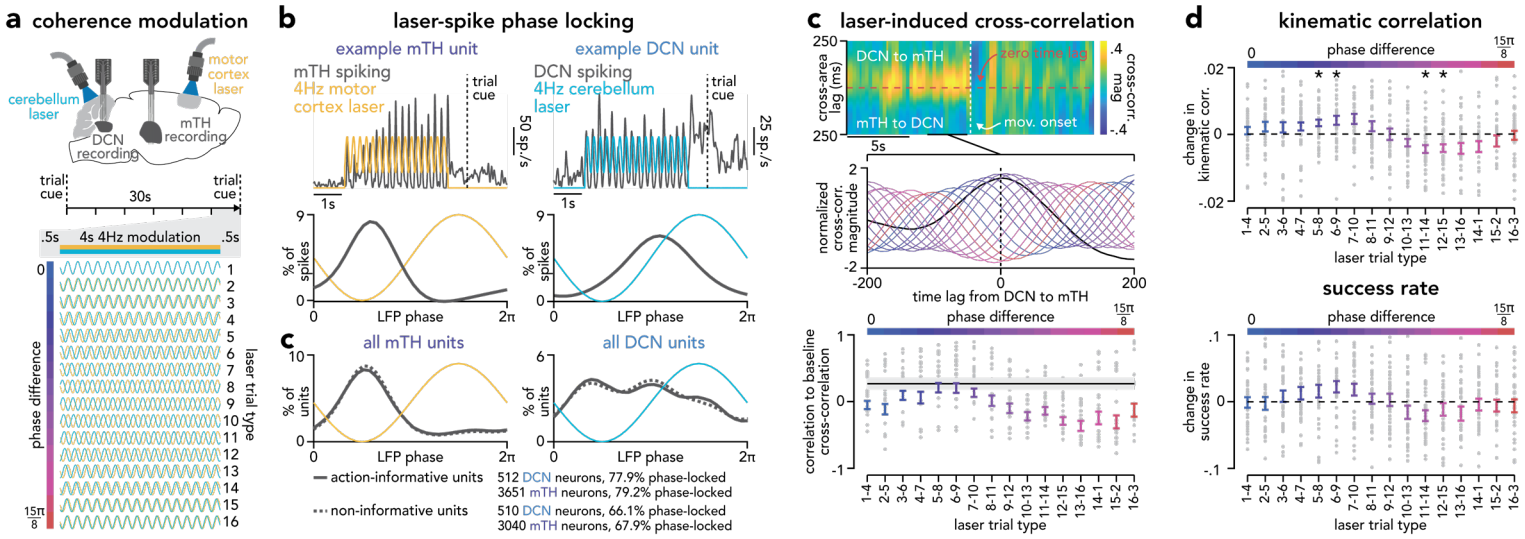

Figure 5: External modulation of cross-area dynamics bidirectionally impacts skilled movement quality.

(a) Schematic of dual-site optogenetic stimulation in VGAT-ChR2 mice. Two optical fibers targeted lobule simplex of the cerebellar cortex and M1, with simultaneous DCN and mTH recordings. On each trial, 4s of 4Hz light stimulation was delivered with one of 16 relative phase offsets, ending 500ms before the trial cue.

(b) Phase locking of mTH and DCN neurons to motor cortex and cerebellum laser, respectively. Top: example mTH and DCN unit spiking during 4Hz cortical and cerebellar stimulation. Middle: corresponding distribution of laser phase for all spikes from example mTH and DCN neurons. Bottom: Phase of phase-locking distribution peak across all recorded mTH and DCN units that were significantly phase-locked to motor cortex and cerebellum laser, respectively. Action-informative and non-informative neural populations are plotted in separate distributions. Percentages indicate the proportion of neurons significantly phase-locked to laser phase in each neural population (Rayleigh test, $P<0.05$, Bonferroni-corrected).

(c) Cross-area mTH and DCN spike-timing relationships during laser stimulation. Top: cross-correlation magnitude across cross-area lag for DCN and mTH neuron pairs. Middle: trial-averaged cross-correlation during 5s pre-movement window for each laser trial type (trial types 1-16 from blue to red) overlaid on trial-averaged cross-correlation from successful non-laser trials in black. Bottom: correlation of trial-average cross-correlation during 5s pre-movement window between groups of laser trial types and trial-averaged cross-correlation from successful non-laser trials on each session (each gray dot represents one session and error bars represent mean±SEM across sessions).

(d) Reach-to-grasp action performance (kinematic correlation and success rate) across groups of laser trial types. Change in success rate (top) and kinematic correlation (bottom) are plotted for groups of laser trial types, relative to the averages across all 16 laser types (each gray dot represents one session and error bars represent mean±SEM across sessions, asterisk denotes significance at $P<0.05$, Bonferroni-corrected, Wilcoxon signed-rank test).

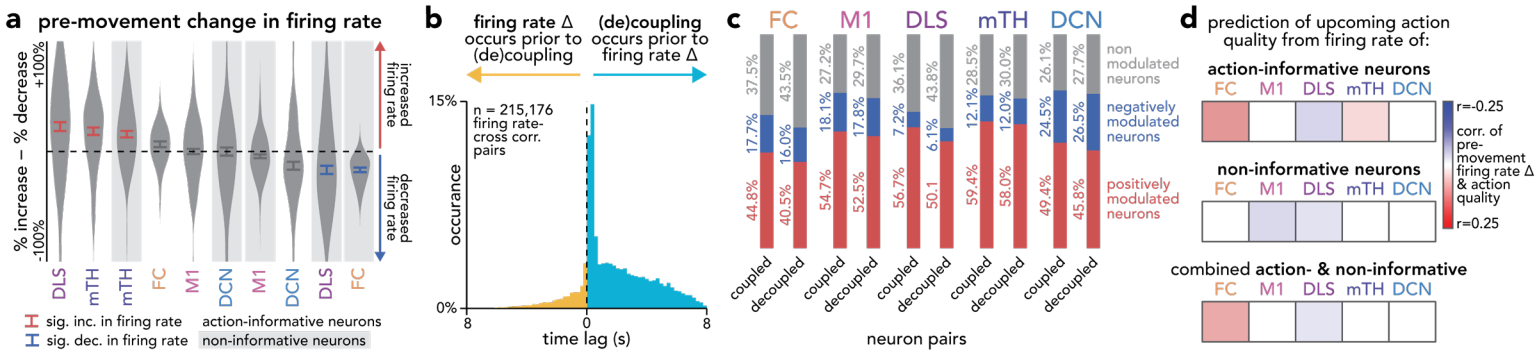

Supplemental Figure 1: Relationship between firing rate changes and network coupling-decoupling.

(a) Difference between the percentage of neurons that increase or decrease in firing rate during the 10s preceding movement. Red and blue bars indicate values significantly above or below zero, shaded bars indicate non-informative neurons ($P < 0.05$, Bonferroni-corrected, one-sample *t*-test; action-informative neurons: FC: $t(38)=2.08$, $P=0.044$, M1: $t(137)=0.19$, $P=0.852$, DLS: $t(127)=5.24$, $P<0.001$, mTH: $t(94)=4.74$, $P<0.001$, DCN: $t(113)=-2.27$, $P=0.025$; non-informative neurons: FC: $t(38)=-8.51$, $P<0.001$, M1: $t(137)=-2.10$, $P=0.037$, DLS: $t(128)=-2.95$, $P=0.004$, mTH: $t(94)=5.60$, $P<0.001$, DCN: $t(113)=-1.59$, $P=0.115$)

(b) Distribution of time lags between initial firing rate changes and start of coupling/decoupling across all neuron pairs.

(c) Proportion of positively modulated, negatively modulated, and non-modulated neurons within coupled and decoupled pairs across brain areas.

(d) Correlations between trial-by-trial action quality (kinematic correlation) and pre-movement changes in firing rate of action-informative neurons (top), non-informative neurons (bottom), or the difference in firing rate changes between action-informative and non-informative neurons (color denotes significance at $P<0.05$, Bonferroni-corrected, Spearman correlation; action-informative neurons: FC: $r=0.013$, $P<0.001$; M1: $r=-0.02$, $P=0.044$; DLS: $r=-0.05$, $P<0.001$; mTH: $r=0.05$, $P<0.001$; DCN: $r=-0.03$, $P=0.014$; non-informative neurons: FC: $r=-0.01$, $P=0.424$; M1: $r=-0.05$, $P<0.001$; DLS: $r=-0.04$, $P=0.001$; mTH: $r=0.02$, $P=0.12$; DCN: $r=-0.02$, $P=0.012$; difference between action-informative and non-informative neurons: FC: $r=0.10$, $P<0.001$; M1: $r=-0.01$, $P=0.40$; DLS: $r=-0.03$, $P=0.002$; mTH: $r=0.02$, $P=0.11$; DCN: $r=0.01$, $P=0.37$).

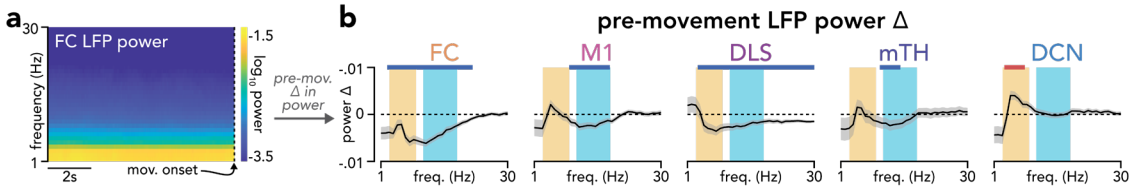

Supplemental Figure 2: Pre-movement LFP power changes.

(a) Example LFP power spectrum in FC aligned to movement onset.

(b) LFP power spectra showing changes in power during the 10s pre-movement period. Yellow and blue bars indicate the 2–8Hz and 10–18Hz frequency ranges, respectively. Red and blue significance bars above each spectrum indicate frequencies with significant increases or decreases, respectively ($P < 0.05$, Wilcoxon signed-rank test, Bonferroni-corrected).

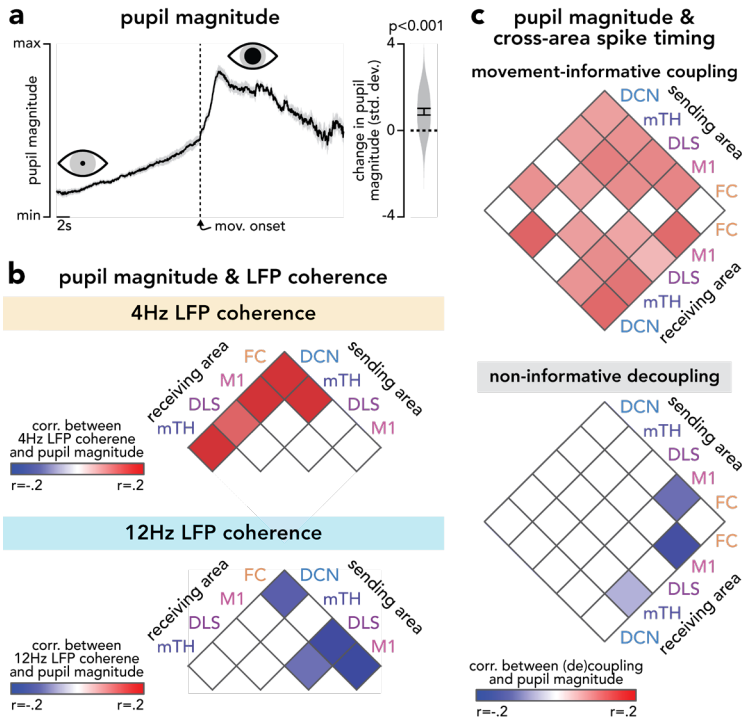

Supplemental Figure 3: Pupil dynamics are correlated with coupling-decoupling and oscillatory changes.

(a) Average pupil magnitude aligned to movement onset (left) and summary of pre-movement pupil magnitude changes across trials (right; $t(29)=5.60$, $P<0.001$).

(b) Matrix of correlations between trial-by-trial pupil magnitude with 4Hz (top) and 12Hz (bottom) LFP coherence across area pairs (color denotes significance at $P<0.05$, Bonferroni-corrected, Spearman correlation; 4Hz LFP coherence: M1/DLS: $r=-0.08$, $P=0.08$; M1/DCN: $r=0.20$, $P<0.001$; M1/mTH: $r=0.12$, $P=0.01$; M1/FC: $r=0.12$, $P=0.01$; DLS/DCN: $r=0.15$, $P=0.001$; DLS/mTH: $r=0.05$, $P=0.25$; DLS/FC: $r=-0.04$, $P=0.46$; DCN/mTH: $r=0.26$, $P<0.001$; DCN/FC: $r=0.28$, $P<0.001$; mTH/FC: $r=0.28$, $P<0.001$;12Hz LFP coherence: M1/DLS: $r=-0.14$, $P=0.003$; M1/DCN: $r=-0.06$, $P=0.18$; M1/mTH: $r=-0.10$, $P=0.03$; M1/FC: $r=-0.26$, $P<0.001$; DLS/DCN: $r=-0.10$, $P=0.03$; DLS/mTH: $r=-0.05$, $P=0.30$; DLS/FC: $r=-0.19$, $P<0.001$; DCN/mTH: $r=-0.01$, $P=0.87$; DCN/FC: $r=-0.16$, $P<0.001$; mTH/FC: $r=-0.01$, $P=0.79$).

(c) Matrix of correlations between trial-by-trial pupil magnitude and action-informative coupling (top) or non-informative decoupling (bottom) for all pairs of sending/receiving areas (color denotes significance at $P<0.05$, Bonferroni-corrected, Spearman correlation; action-informative: M1 to DLS: $r=0.09$, $P<0.001$; DLS to M1: $r=0.11$, $P<0.001$; M1 to DCN: $r=0.11$, $P<0.001$; DCN to M1: $r=0.10$, $P<0.001$; M1 to mTH: $r=0.11$, $P<0.001$; mTH to M1: $r=0.12$, $P<0.001$; M1 to FC: $r=0.12$, $P<0.001$; FC to M1: $r=0.14$, $P<0.001$; DLS to DCN: $r=0.05$, $P=0.015$; DCN to DLS: $r=0.06$, $P=0.004$; DLS to mTH: $r=0.10$, $P<0.001$; mTH to DLS: $r=0.09$, $P<0.001$; DLS to FC: $r=0.12$, $P<0.001$; FC to DLS: $r=0.07$, $P=0.001$; DCN to mTH: $r=0.11$, $P<0.001$; mTH to DCN: $r=0.15$, $P<0.001$; DCN to FC: $r=0.09$, $P<0.001$; FC to DCN: $r=0.15$, $P<0.001$; mTH to FC: $r=0.11$, $P<0.001$; FC to mTH: $r=0.13$, $P<0.001$; non-informative: M1 to DLS: $r=-0.00$, $P=0.83$; DLS to M1: $r=-0.05$, $P=0.02$; M1 to DCN: $r=-0.04$, $P=0.07$; DCN to M1: $r=0.00$, $P=0.95$; M1 to mTH: $r=-0.01$, $P=0.72$; mTH to M1: $r=0.03$, $P=0.14$; M1 to FC: $r=-0.14$, $P<0.001$; FC to M1: $r=-0.19$, $P<0.001$; DLS to DCN: $r=-0.02$, $P=0.39$; DCN to DLS: $r=-0.01$, $P=0.64$; DLS to mTH: $r=-0.03$, $P=0.19$; mTH to DLS: $r=0.04$, $P=0.04$; DLS to FC: $r=-0.04$, $P=0.10$; FC to DLS: $r=-0.04$, $P=0.08$; DCN to mTH: $r=0.01$, $P=0.78$; mTH to DCN: $r=0.02$, $P=0.41$; DCN to FC: $r=-0.03$, $P=0.17$; FC to DCN: $r=-0.02$, $P=0.47$; mTH to FC: $r=-0.00$, $P=0.98$; FC to mTH: $r=-0.08$, $P<0.001$).

Methods

Animals. All experimental procedures were approved by the Institutional Animal Care and Use Committee at the University of North Carolina at Chapel Hill. Wild-type (WT) and *Slc32a1-ChR2(H134R)*-EYFP mice[62] (The Jackson Laboratory Strain #014548), aged 12-40 weeks of both sexes were studied.

Reach-to-grasp task. Mice were implanted with a 3D-printed headpost (Formlabs), food-restricted to 75–85% baseline, and trained on a head-fixed single-pellet reach-to-grasp task adapted from prior work[12,16]. Trials occurred every 30s (with inter-trial-interval perturbations at 20s and 40s). On each trial, pellet presentation was paired with an auditory cue, and behavior was captured by two synchronized infrared cameras (PointGrey Flea3) at 500Hz using BIAS (IO Rodeo) with event timing from WaveSurfer (Adam Taylor; Janelia Research Campus). Videos from the front and side views were calibrated with the Caltech Camera Calibration Toolbox. Hand and digit kinematics (first and third digits) were tracked using the Animal Part Tracker (Kristin Branson; Janelia Research Campus). Post-processing was performed with custom MATLAB scripts to detect relevant time points: movement onset (first initiation of hand motion after the cue toward the pellet), maximum velocity (peak hand speed during the outward reach), hand open (peak of grip aperture), grab (onset of digit closure following the hand-open peak), and supination (first sustained increase in hand rotation angle bringing the palm surface toward the mouth). Continuous kinematic features were also quantified: hand velocity, grip aperture (distance between first and third digits), and supination angle (hand rotation angle). Performance metrics included success rate, reaction time (cue to movement onset), kinematic correlation (Pearson correlation between each trial's velocity/acceleration/grip aperture and the session mean of successful trials), and trajectory variance (across-trial variance of the 3D hand trajectory). Action quality was defined as the correlation of each trial's kinematics with the mean kinematics of successful trials within that session.

Multi-site neurophysiology. We performed simultaneous 4-shank Neuropixels 2.0[63] recordings across five interconnected nodes of the motor network: frontal cortex (FC, coordinates: +1 to +2.8mm AP, +0.6 to +1.0mm ML), primary motor cortex (M1, coordinates: -0.1 to +0.7mm AP, +0.4 to +2.2mm ML), dorsolateral striatum (DLS, coordinates: -0.1 to +0.7mm AP, +1.0 to +2.6mm ML), motor thalamus (mTH; coordinates: −1.0 to −2.0mm AP, +0.3 to +2.0mm ML), and interposed nucleus of the deep cerebellar nuclei (DCN, coordinates: −5.75 to −6.5mm AP, +1.1 to +2.6mm ML) (**Figure 1e**). Four probes were used with M1/DLS recorded on the same probe. Shanks were coated in DiI stain to find electrode track positions in post hoc histology. Signals were acquired using SpikeGLX at 30 kHz. Spike sorting was performed using Kilosort 2.5[64] with manual curation in Phy[65], aided by Bombcell[66] for automated quality control. Units localized outside the anatomical coordinates above were excluded from analysis. Local field potentials (LFPs) were extracted using custom MATLAB scripts that low-pass filtered raw data at 300Hz (fourth-order Butterworth) and downsampled to 1 kHz. Four channels (every 48th channel) were extracted from each shank of the 4-shank Neuropixels 2.0 probes (resulting in 16 total LFP channels per Neuropixels probe). Within each area, LFP channels were median referenced.

Optogenetics. In *Slc32a1-ChR2(H134R)-EYFP* mice[62] (*VGAT-ChR2*), we placed two optical fibers targeting lobule simplex of the cerebellar cortex (projecting to the interposed nucleus of the DCN) and M1. Fibers (200µm, NA 0.39, Thorlabs) were positioned on the skull surface at -6.3mm AP +1.5ML (lobule simplex) and +0.7AP +2ML (M1) and coupled to a 473nm laser (Laserglow) via patch cords. Output power was measured at the fiber tip each session and adjusted to elicit reliable neuronal entrainment (range: 10-50mW). During recordings, we simultaneously captured spikes in DCN and mTH to quantify phase-locking and cross-area spike-timing. Each session began with control (no-light) trials, followed by repeated cycles of 16 stimulation trials. On every stimulation trial, both sites received 4s of 4Hz sinusoidal light, ending 500ms before the behavioral cue. The relative phase between cerebellar and cortical pulse trains varied across 16 offsets (**Figure 5a**).

Action modulation and timing. To quantify action-modulation, we smoothed a 1ms binned spike train with a Gaussian kernel (σ = 100ms) and then trial-averaged. We z-scored each unit's movement activity using a pre-movement baseline from −4000 to −1000ms relative to movement onset. Units were classified as modulated if the magnitude of activity in a movement-aligned window (−250 to +500ms) exceeded the activity from a preceding window (−1000 to −250ms before movement onset) by a factor >2. Modulation sign was determined by whether the z-scored activity during the movement window showed a net increase (positively modulated) or decrease (negatively modulated) relative to pre-movement baseline. Modulation timing was defined as the first time bin within −200 to +500ms relative to movement onset to cross a fixed z-threshold: +3 SD for positively modulated units and −2 SD for negatively modulated units.

Action-informative and non-informative neuron classification. To identify neurons encoding movement-relevant information, we computed Shannon information (direct method[42,67]) between each neuron's binned firing rate (5ms bins, discretized into four equipopulated levels) and kinematics (acceleration and grip aperture, five bins). For each neuron, we evaluated neural-to-behavioral lags from −250 to 0ms in 5ms steps (50 evaluations), measuring information in a peri-movement epoch (0–500ms post-movement onset). Significance was assessed against a trial-shuffled distribution (100 shuffles) generated by permuting trial order and recomputing information. Neurons exceeding the 95th percentile of this shuffled distribution for ≥5 consecutive lags and doing so for ≥10 total lags were designated action-informative, all others were non-informative. Information timing was defined as the earliest lag that a neuron encoded significant information about either grip aperture or reach acceleration.

Cross-area coupling and decoupling. We defined coupling and decoupling based on the consistency of spike-timing relationships. Spike trains were binned at 5ms, Gaussian-smoothed ($\sigma = 100$ms), and median-centered across trials. We computed trial-wise cross-correlations for all cross-area neuron pairs using 500ms windows sliding across −10 to +10s around movement onset in 100ms jumps, evaluating cross-area time lags from −250 to +250ms. Coupling was defined as an increase in the peak cross-correlation magnitude during the pre-movement period (−10 to 0s preceding movement onset), decoupling was defined as a decrease. Pairwise directionality was assigned from the lag of the correlation peak, indicating which area's spikes led or lagged the other. Session-level statistics summarized, for each directed area pair, the fraction of neuron pairs that significantly increased (coupled) or decreased (decoupled) in correlation magnitude during the pre-movement period. To relate these dynamics to behavioral performance, we computed the mean pre-movement change in peak cross-correlation across all action-informative pairs that coupled and the mean pre-movement change across all non-informative pairs that decoupled. These measures were correlated with trial-by-trial action quality, quantified as the correlation of each individual trial's kinematics to the mean kinematics of successful actions across that recording session.

LFP analysis. Local field potentials (LFPs) were analyzed using the Chronux toolbox[68], using functions *mtspecgramc* and *cohgramc*. We computed trial-by-trial LFP coherence between all pairs of recorded areas over a −10 to 0s pre-movement window. Pre-movement power and coherence dynamics were quantified as the difference between power/coherence spectra averaged across −2 to 0s and −10 to −8s prior to movement onset. The relationship between LFP coherence and coupling-decoupling was computed by measuring 4Hz coherence between DCN and mTH or 12Hz coherence between FC and M1, and correlating these trial-by-trial measures to corresponding pre-movement cross-correlation magnitude among action-informative neuron pairs that coupled or non-informative pairs that decoupled. To assess single-unit phase locking, LFPs were filtered between 2-8Hz with a zero-phase 2nd-order Butterworth filter, and instantaneous phase was extracted via the Hilbert transform. The phase of each spike occurring 2.5–5 s before movement onset was pooled across trials, and circular non-uniformity was tested with the Rayleigh test to determine significant phase locking.

Pupillometry. Pupil area was extracted from high-speed videos, z-scored within session, and aligned to movement onset. Trial-by-trial pupil magnitude during the −5 s to 0 s pre-movement window was then correlated with multiple neural features to identify a non-invasive marker of network engagement. These included mean 4Hz and 12Hz LFP coherence across all recorded area pairs, the pre-movement change in cross-correlation magnitude among action-informative neuron pairs that coupled, and the change among non-informative pairs that decoupled.

References

1. Palkovits, M., Mezey, E., Hámori, J. & Szentágothai, J. Quantitative histological analysis of the cerebellar nuclei in the cat. I. Numerical data on cells and on synapses. *Exp. Brain Res.* **28**, 189–209 (1977).
2. Napper, R. M. & Harvey, R. J. Number of parallel fiber synapses on an individual Purkinje cell in the cerebellum of the rat. *J. Comp. Neurol.* **274**, 168–177 (1988).
3. Braitenberg, V. & Schuz, A. *Cortex: Statistics and Geometry of Neuronal Connectivity*. (Springer, Berlin, Germany, 2012). doi:10.1007/978-3-662-03733-1.
4. Kincaid, A. E., Zheng, T. & Wilson, C. J. Connectivity and convergence of single corticostriatal axons. *J. Neurosci.* **18**, 4722–4731 (1998).
5. Markram, H. *et al.* Reconstruction and simulation of neocortical microcircuitry. *Cell* **163**, 456–492 (2015).
6. MICrONS Consortium. Functional connectomics spanning multiple areas of mouse visual cortex. *Nature* **640**, 435–447 (2025).
7. Stringer, C. *et al.* Spontaneous behaviors drive multidimensional, brainwide activity. *Science* **364**, 255 (2019).

8. Salkoff, D. B., Zagha, E., McCarthy, E. & McCormick, D. A. Movement and Performance Explain Widespread Cortical Activity in a Visual Detection Task. *Cereb. Cortex* **30**, 421–437 (2020).
9. Musall, S., Kaufman, M. T., Juavinett, A. L., Gluf, S. & Churchland, A. K. Single-trial neural dynamics are dominated by richly varied movements. *Nat. Neurosci.* **22**, 1677–1686 (2019).
10. International Brain Laboratory *et al.* A brain-wide map of neural activity during complex behaviour. *Nature* **645**, 177–191 (2025).
11. Whishaw, I. Q., O'Connor, W. T. & Dunnett, S. B. The contributions of motor cortex, nigrostriatal dopamine and caudate-putamen to skilled forelimb use in the rat. *Brain* **109 (Pt 5)**, 805–843 (1986).
12. Guo, J.-Z. *et al.* Cortex commands the performance of skilled movement. *Elife* **4**, e10774 (2015).
13. Lemke, S. M., Ramanathan, D. S., Guo, L., Won, S. J. & Ganguly, K. Emergent modular neural control drives coordinated motor actions. *Nat. Neurosci.* **22**, 1122–1131 (2019).
14. Veuthey, T. L., Derosier, K., Kondapavulur, S. & Ganguly, K. Single-trial cross-area neural population dynamics during long-term skill learning. *Nat. Commun.* **11**, 4057 (2020).
15. Saiki-Ishikawa, A. *et al.* Hierarchy between forelimb premotor and primary motor cortices and its manifestation in their firing patterns. *Elife* **13**, (2025).
16. Sauerbrei, B. A. *et al.* Cortical pattern generation during dexterous movement is input-driven. *Nature* **577**, 386–391 (2020).
17. Becker, M. I. & Person, A. L. Cerebellar Control of Reach Kinematics for Endpoint Precision. *Neuron* **103**, 335-348.e5 (2019).
18. Guo, J.-Z. *et al.* Disrupting cortico-cerebellar communication impairs dexterity. *Elife* **10**, (2021).
19. Wagner, M. J. *et al.* Shared Cortex-Cerebellum Dynamics in the Execution and Learning of a Motor Task. *Cell* **177**, 669-682.e24 (2019).
20. Lemke, S. M., Celotto, M., Maffulli, R., Ganguly, K. & Panzeri, S. Information flow between motor cortex and striatum reverses during skill learning. *Curr. Biol.* **34**, 1831-1843.e7 (2024).
21. Balzani, E., Noel, J. P., Herrero-Vidal, P., Angelaki, D. E. & Savin, C. A probabilistic framework for task-aligned intra- and inter-area neural manifold estimation. *arXiv [q-bio.NC]* (2022).
22. Sani, O. G., Pesaran, B. & Shanechi, M. M. Dissociative and prioritized modeling of behaviorally relevant neural dynamics using recurrent neural networks. *Nat. Neurosci.* **27**, 2033–2045 (2024).
23. Sani, O. G., Abbaspourazad, H., Wong, Y. T., Pesaran, B. & Shanechi, M. M. Modeling behaviorally relevant neural dynamics enabled by preferential subspace identification. *Nat. Neurosci.* **24**, 140–149 (2021).
24. Azim, E., Jiang, J., Alstermark, B. & Jessell, T. M. Skilled reaching relies on a V2a propriospinal internal copy circuit. *Nature* **508**, 357–363 (2014).
25. Yang, W., Kanodia, H. & Arber, S. Structural and functional map for forelimb movement phases between cortex and medulla. *Cell* **186**, 162-177.e18 (2023).
26. Ruder, L. *et al.* A functional map for diverse forelimb actions within brainstem circuitry. *Nature* **590**, 445–450 (2021).
27. Quarta, E. *et al.* Distributed and localized dynamics emerge in the mouse neocortex during reach-to-grasp behavior. *J. Neurosci.* **42**, 777–788 (2022).
28. Tombaz, T. *et al.* Action representation in the mouse parieto-frontal network. *Sci. Rep.* **10**, 5559 (2020).
29. Jeannerod, M. The timing of natural prehension movements. *J. Mot. Behav.* **16**, 235–254 (1984).
30. Whishaw, I. Q., Pellis, S. M. & Gorny, B. P. Skilled reaching in rats and humans: evidence for parallel development or homology. *Behav. Brain Res.* **47**, 59–70 (1992).
31. Sacrey, L.-A. R., Alaverdashvili, M. & Whishaw, I. Q. Similar hand shaping in reaching-for-food (skilled reaching) in rats and humans provides evidence of homology in release, collection, and manipulation movements. *Behav. Brain Res.* **204**, 153–161 (2009).
32. Alstermark, B. & Isa, T. Circuits for skilled reaching and grasping. *Annu. Rev. Neurosci.* **35**, 559–578 (2012).
33. Dum, R. P. & Strick, P. L. Frontal lobe inputs to the digit representations of the motor areas on the lateral surface of the hemisphere. *J. Neurosci.* **25**, 1375–1386 (2005).
34. Hausmann, F. S., Barrett, J. M., Martin, M. E., Zhan, H. & Shepherd, G. M. G. Axonal barcode analysis of pyramidal tract projections from mouse forelimb M1 and M2. *J. Neurosci.* **42**, 7733–7743 (2022).
35. Dudman, J. T. & Gerfen, C. R. The Basal Ganglia. in *The Rat Nervous System* 391–440 (Elsevier, 2015).
36. Aoki, S. *et al.* An open cortico-basal ganglia loop allows limbic control over motor output via the nigrothalamic pathway. *Elife* **8**, (2019).
37. Hintzen, A., Pelzer, E. A. & Tittgemeyer, M. Thalamic interactions of cerebellum and basal ganglia. *Brain Struct. Funct.* **223**, 569–587 (2018).
38. Low, A. Y. T. *et al.* Precision of discrete and rhythmic forelimb movements requires a distinct neuronal subpopulation in the interposed anterior nucleus. *Cell Rep.* **22**, 2322–2333 (2018).
39. Houck, B. D. & Person, A. L. Cerebellar premotor output neurons collateralize to innervate the cerebellar cortex: Collateral pathway in mouse cerebellum. *J. Comp. Neurol.* **523**, 2254–2271 (2015).
40. Küper, M. *et al.* Lesions of the dentate and interposed nuclei are associated with impaired prehension in cerebellar patients. *Neurosci. Lett.* **499**, 132–136 (2011).
41. Shannon, C. E. A mathematical theory of communication. *Bell Syst. tech. j.* **27**, 379–423 (1948).

42. Quian Quiroga, R. & Panzeri, S. Extracting information from neuronal populations: information theory and decoding approaches. *Nat. Rev. Neurosci.* **10**, 173–185 (2009).
43. Pfurtscheller, G. & Lopes da Silva, F. H. Event-related EEG/MEG synchronization and desynchronization: basic principles. *Clin. Neurophysiol.* **110**, 1842–1857 (1999).
44. van Wijk, B. C. M. *et al.* Low-beta cortico-pallidal coherence decreases during movement and correlates with overall reaction time. *Neuroimage* **159**, 1–8 (2017).
45. Fries, P. A mechanism for cognitive dynamics: neuronal communication through neuronal coherence. *Trends Cogn. Sci.* **9**, 474–480 (2005).
46. Fries, P. Rhythms for Cognition: Communication through Coherence. *Neuron* **88**, 220–235 (2015).
47. Khanna, P. & Carmena, J. M. Beta band oscillations in motor cortex reflect neural population signals that delay movement onset. *Elife* **6**, (2017).
48. Reimer, J. *et al.* Pupil fluctuations track rapid changes in adrenergic and cholinergic activity in cortex. *Nat. Commun.* **7**, 13289 (2016).
49. Perich, M. G. *et al.* Motor cortical dynamics are shaped by multiple distinct subspaces during naturalistic behavior. *bioRxiv* 2020.07.30.228767 (2020) doi:10.1101/2020.07.30.228767.
50. Miller, E. K. & Cohen, J. D. An integrative theory of prefrontal cortex function. *Annu. Rev. Neurosci.* **24**, 167–202 (2001).
51. Halassa, M. M. & Kastner, S. Thalamic functions in distributed cognitive control. *Nat. Neurosci.* **20**, 1669–1679 (2017).
52. Joshi, S., Li, Y., Kalwani, R. M. & Gold, J. I. Relationships between pupil diameter and neuronal activity in the locus coeruleus, colliculi, and cingulate cortex. *Neuron* **89**, 221–234 (2016).
53. Tanji, J. & Evarts, E. V. Anticipatory activity of motor cortex neurons in relation to direction of an intended movement. *J. Neurophysiol.* **39**, 1062–1068 (1976).
54. Churchland, M. M., Santhanam, G. & Shenoy, K. V. Preparatory activity in premotor and motor cortex reflects the speed of the upcoming reach. *J. Neurophysiol.* **96**, 3130–3146 (2006).
55. Afshar, A. *et al.* Single-trial neural correlates of arm movement preparation. *Neuron* **71**, 555–564 (2011).
56. Guo, Z. V. *et al.* Maintenance of persistent activity in a frontal thalamocortical loop. *Nature* **545**, 181–186 (2017).
57. Catanese, J. & Jaeger, D. Premotor ramping of thalamic neuronal activity is modulated by nigral inputs and contributes to control the timing of action release. *J. Neurosci.* **41**, 1878–1891 (2021).
58. London, T. D. *et al.* Coordinated ramping of dorsal striatal pathways preceding food approach and consumption. *J. Neurosci.* **38**, 3547–3558 (2018).
59. Riehle, A., Grün, S., Diesmann, M. & Aertsen, A. Spike synchronization and rate modulation differentially involved in motor cortical function. *Science (New York, N.Y.)* vol. 278 1950–1953 (1997).
60. Torre, E. *et al.* Synchronous spike patterns in macaque motor cortex during an instructed-delay reach-to-grasp task. *J. Neurosci.* **36**, 8329–8340 (2016).
61. Fornito, A., Zalesky, A. & Breakspear, M. The connectomics of brain disorders. *Nat. Rev. Neurosci.* **16**, 159–172 (2015).
62. Zhao, S. *et al.* Cell type–specific channelrhodopsin-2 transgenic mice for optogenetic dissection of neural circuitry function. *Nat. Methods* **8**, 745–752 (2011).
63. Steinmetz, N. A. *et al.* Neuropixels 2.0: A miniaturized high-density probe for stable, long-term brain recordings. *Science* **372**, (2021).
64. Pachitariu, M., Sridhar, S. & Stringer, C. Solving the spike sorting problem with Kilosort. *bioRxiv* 2023.01.07.523036 (2023) doi:10.1101/2023.01.07.523036.
65. Rossant, C. *et al.* Spike sorting for large, dense electrode arrays. *Nat. Neurosci.* **19**, 634–641 (2016).
66. Fabre, J. M. J., van Beest, E. H., Peters, A. J., Carandini, M. & Harris, K. D. Bombcell: automated curation and cell classification of spike-sorted electrophysiology data. *Zenodo* (2023).
67. Lorenz, G. M. *et al.* MINT: A toolbox for the analysis of multivariate neural information coding and transmission. *PLoS Comput. Biol.* **21**, e1012934 (2025).
68. Bokil, H., Andrews, P., Kulkarni, J. E., Mehta, S. & Mitra, P. P. Chronux: a platform for analyzing neural signals. *J. Neurosci. Methods* **192**, 146–151 (2010).